Supporting Information

Dark Photocatalysis: Storage of Solar Energy in Carbon Nitride for Time-Delayed Hydrogen Generation

Vincent Wing-hei Lau[+], Daniel Klose[+], Hatice Kasap[+], Filip Podjaski, Marie-Claire Pignié, Erwin Reisner,* Gunnar Jeschke,* and Bettina V. Lotsch*

anie_201608553_sm_miscellaneous_information.pdf

Supplementary Information

Experimental Section

NCN-CN$_x$ was prepared from melon and KSCN and structurally characterised as reported previously.[1] For characterisation of the NCN-CN$_x$ as a suspension, the powder was dispersed in the solvent specified and sonicated, yielding a suspension that has colloidal stability for some minutes. To manifest the radical state, the suspension was deaerated by bubbling with argon or using solvents subjected to multiple freeze-pump-thaw cycles. Suspensions in EPR capillaries were deaerated by bubbling with nitrogen and five freeze-pump-thaw cycles. Fourier transform infrared (FTIR) spectroscopy was performed on a PerkinElmer UATR TWO spectrometer equipped with a diamond crystal. Ultraviolet-visible (UV-Vis) transmission spectra of the NCN-CN$_x$ suspension were collected on a Cary 60 UV-Vis spectrometer in a quartz cuvette with a Schlenk tap for oxygen-free handling.

The photocatalytic experiments were conducted in a glass photoreactor with a quartz window on the top and thermostated at 25 °C, as described in our previous works;[1-2] all glassware used for the experiments was soaked overnight in aqua regia. A standard experiment for dark hydrogen evolution involved irradiating under AM1.5 conditions a deaerated suspension of NCN-CN$_x$ (20 mg) and 4-MBA (24 mg, equivalent to a concentration of 10 µM) in phosphate buffer (20 mL, pH 7, 1 M), unless otherwise stated. The platinum co-catalyst (50 µL of 1000 ppm aqueous colloidal solution, Aldrich) was injected using a gas-tight syringe using Schlenk technique. For the dark hydrogen evolution experiments, care was taken to eliminate irradiation by stray light by wrapping the reactor in aluminium foil and to avoid introducing air during injection of the co-catalyst by using the stringent Schlenk technique. The pH of the reaction solution did not change from its initial value of pH 7 at the end of the dark photocatalysis experiment. For wavelength-dependent measurements, band pass filters centred at 400, 450 and 500 nm with a full width at half maximum of 40 nm from Thorlab were employed.

Photoelectrochemical measurements were performed in a closed glass reactor equipped with a quartz window for illumination. Phosphate buffer (1 M, pH 6.3) was used as supporting electrolyte; a Ag/AgCl electrode in saturated KCl solution was used as the reference electrode (0.197V vs SHE) and a Pt wire as counter electrode. The electrolyte solution was purged with >99% pure N$_2$ prior to every measurement through a porous glass frit to remove dissolved oxygen. Measurements were recorded using an Ivium CompactStat potentiostat controlled with the IviumSoft software. The irradiation source was a Sciencetech LightLine A4 solar simulator (class AAA) based on the ASTM standard G138. The intensity was measured at the place of the sample by a calibrated Thorlabs S310C thermal power meter and further confirmed by a calibrated Ocean Optics USB4000 spectrometer. The working electrodes were prepared as follows. 10 mg of NCN-CNx was sonicated in 10 mL deionized water for 2 h in an ice bath. 10 µL of this suspension was drop cast onto FTO slides (5×5 mm, contacted to copper wires with silver paste), dried at 60 °C, and then sealed with epoxy (3M Scotch-Weld DP410).

EPR experiments were performed on an Elexsys E500 CW EPR spectrometer (Bruker) at X band frequencies of about 9.6 GHz and on an Elexsys E680 CW/pulsed EPR spectrometer (Bruker) at W-band frequencies of about 94.2 GHz at a temperature of 50 K using an Oxford Instruments flow cryostat. For W-band EPR, the sample was filled in a 0.7 mm O.D. capillary and irradiated for 2 min or 1 hour using an OmniCure S2000 UV lamp (Mercury lamp, nominal 200W) with the capillary centred inside the X-Band EPR resonator, 2.5 cm from the end of the lamp's optical fiber. CW EPR was

measured under non-saturating conditions with 47 dB attenuation of the nominally 2 W microwave power from a home-built W-band microwave bridge that replaces the original Bruker W-band bridge. A modulation amplitude of 0.03 mT (peak-to-peak) was applied. We found that determination of exact g values required the use of an internal reference, for which we used MgO containing trace amounts of Mn(II). Deviations between the experimental and simulated line shape (see Figure 2 in the main text) stem from neglect of all but the strongest hyperfine coupling and from using a Gaussian strain model, whereas the line shape indicates that strain near $g_x = 2.00246$ is asymmetric with a broader wing towards smaller values.

Transverse and longitudinal relaxation times of the electron spins were measured by two-pulse echo decay and inversion recovery experiments, respectively. A phase memory time of only 512 ns at a temperature of 50 K was observed by primary two-pulse echo decay at W-band frequencies. The decay is strongly non-exponential with quite significant echo intensity still existing after 6 μs (data not shown). Longitudinal relaxation is also strongly non-exponential with initial magnetization recovery of a fraction $1/e$ within 60 μs in an inversion recovery experiment and with the decay still being incomplete after 12 ms (data not shown).

The HYSCORE spectra were taken with the standard $\pi/2$-τ-$\pi/2$-t_1-π-t_2-$\pi/2$-τ-echo sequence and a standard 8-step phase cycle with pulse lengths of 24 ns for the $\pi/2$ and 20 ns for the π pulse. The sequence was repeated with a delay of 2.5 ms. Starting times of 140 ns for t_1 and t_2 with time increments Δt = 16 ns were used. HYSCORE raw data were processed by correcting the baseline of the time traces in both dimensions with a second-order polynomial function. After a Lorentz-Gaussian transformation, the traces were apodized with a Hamming function and zero-filled to the next power of 2 as a numbers of points (2048 points). Finally, 2D Fourier transformation was applied to the data matrix and the absolute value of the spectrum plotted using MATLAB software. Three magnitude spectra measured with interpulse delays τ of 124, 144, and 164 ns were summed in order to eliminate blind-spot effects. HYSCORE spectra were measured at two observer fields (see Figure S1) to reduce loss of correlation peaks by orientation selection. For the same reason, simulations were performed with an isotropic g value. Some features seen in the simulations are not observed experimentally and relative intensities differ between experiment and simulation. This can be attributed to remaining blind spot suppression after adding three HYSCORE spectra with interpulse delays 124, 144, and 164 ns and to pulse non-ideality that is not considered in the simulations.
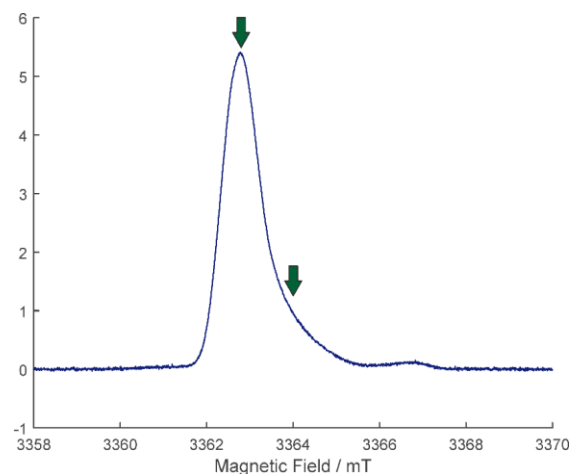
Figure S1 Field-swept echo-detected EPR spectrum of light-irradiated (1 h) NCN-CN$_x$ obtained at W band. The green arrows denote the two observer fields where HYSCORE spectra were taken.

The interpulse delays τ for HYSCORE were selected on the basis of a series of three-pulse electron spin echo envelope modulation (ESEEM) experiments (Figure S2), which showed that all ESEEM frequencies are covered at these three delays. The ESEEM traces exhibit a relatively low modulation depth for a case where the hyperfine coupling is close to exact cancellation of the nuclear Zeeman interaction. This indicates that not all radicals feature the large ^{14}N hyperfine coupling that is observed by ESEEM and HYSCORE.
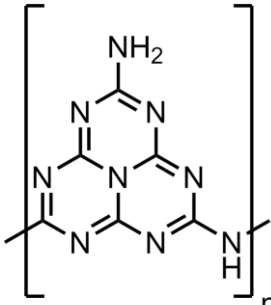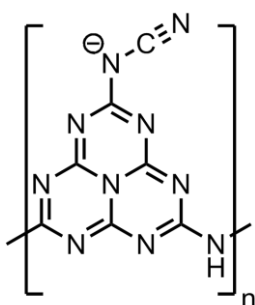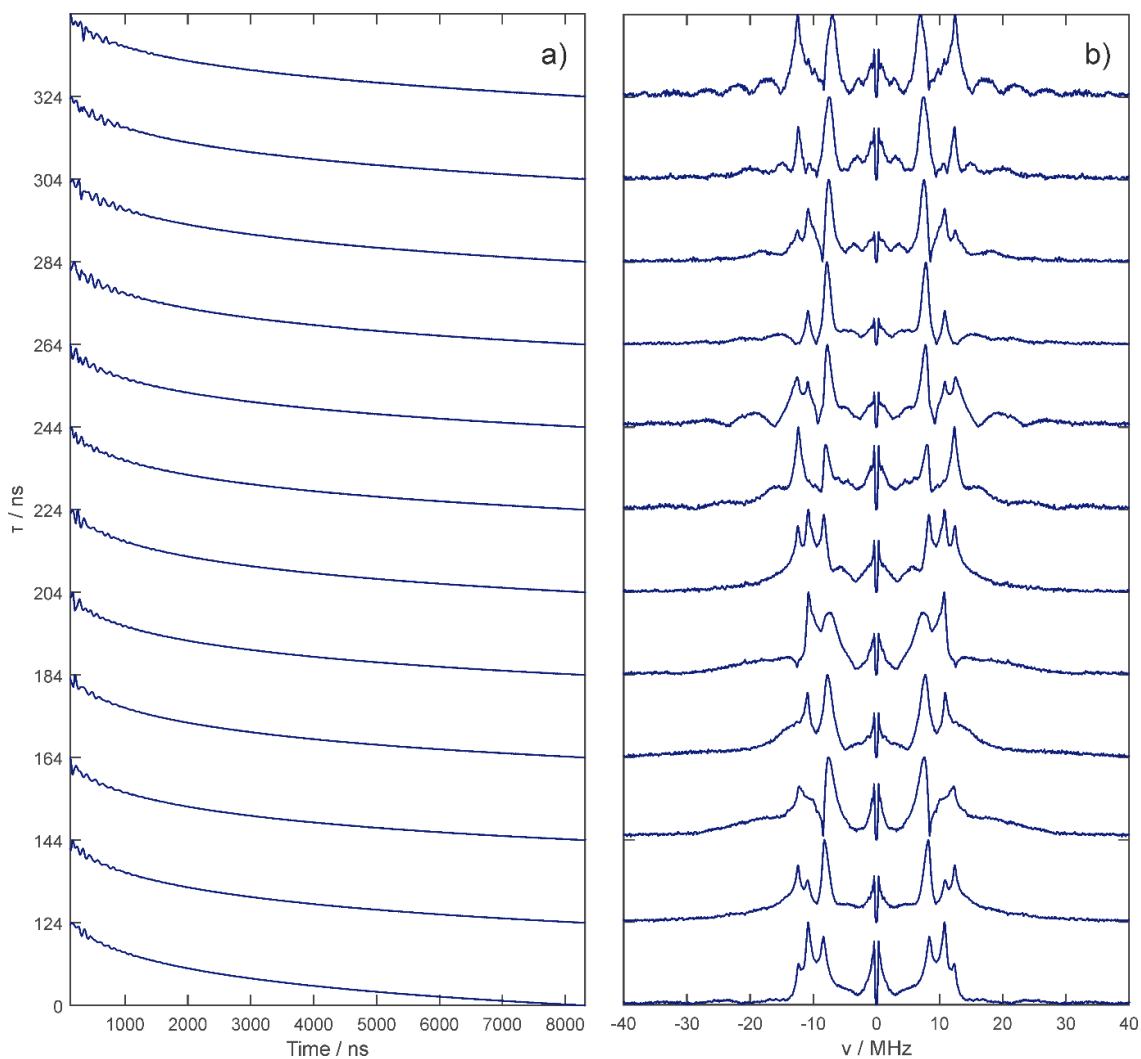
Figure S2 W-band three-pulse ESEEM of of light-irradiated (1 h) NCN-CN$_x$. a) Primary data. b) ESEEM spectra obtained by 6th-order polynomial background correction, Hamming apodization, zero-filling to twice the original number of data points, Fourier transformation, and computation of the magnitude spectrum. Spectra at large interpulse delays τ clearly exhibit blind spot behaviour of the broad signal. This broad signal as well as all prominent narrow signals are fully covered by the three spectra taken at interpulse delays τ = 124, 144, and 164 ns.

Table S1 Structural properties and optical gaps of the materials in this work

Notation	Melon	NCN-CN$_x$
Molecular Weight (g mol^{-1})	201.15	249.01
Formula	C$_a$N$_9$H$_3$	[K$_{0.6}$H$_{0.4}$]$^+$[C$_7$N$_9$H]$^-$*
Optical gap (eV)	2.69	2.69

*Cation content determined by ICP-AES elemental analysis

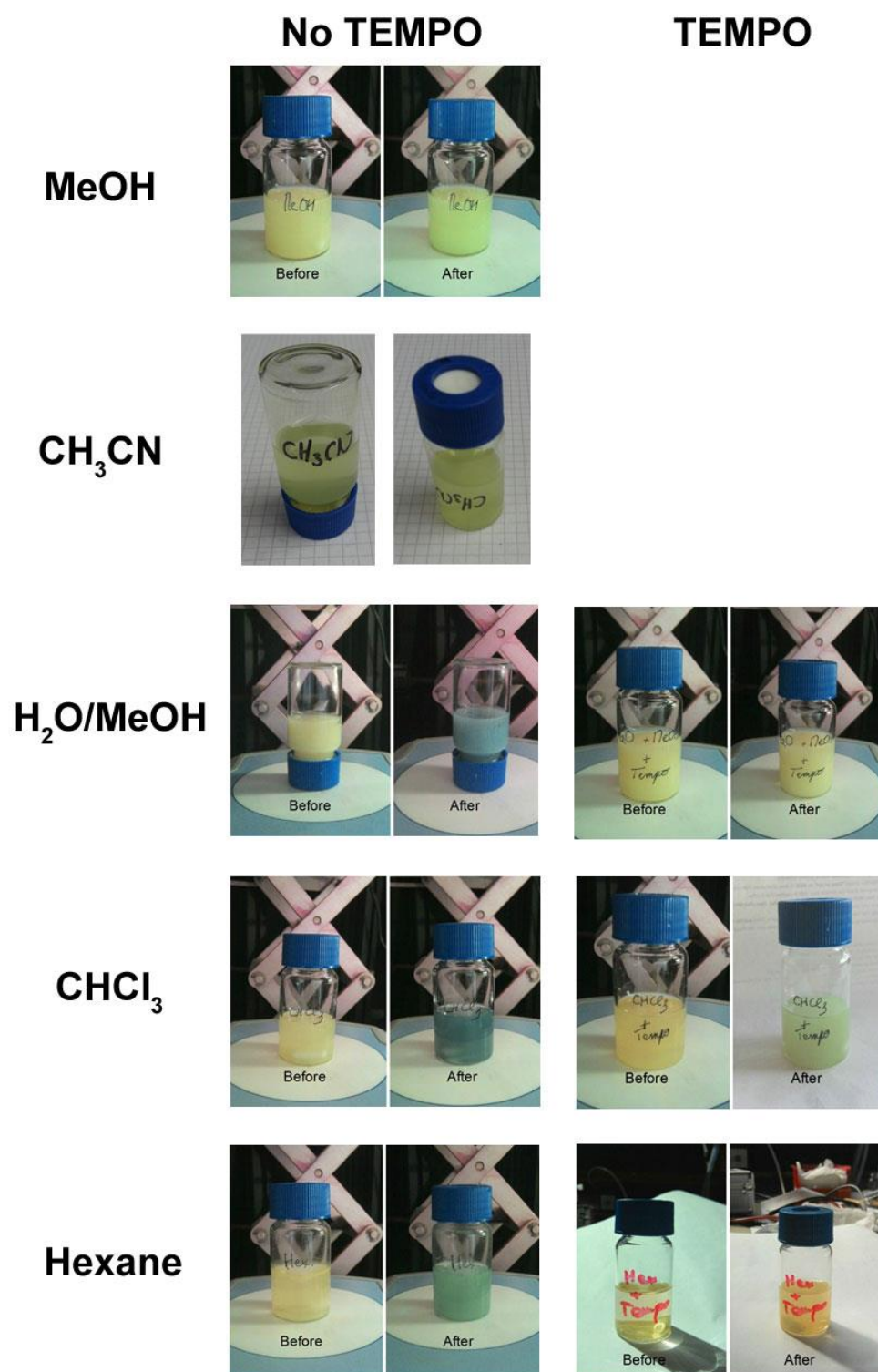# Preliminary tests of NCN-CN$_x$ for colour change

Figure S3 Deaerated NCN-CN$_x$ suspensions in different solvents before and after irradiation. Further tests with TEMPO were made for the suspensions that exhibited colour change.

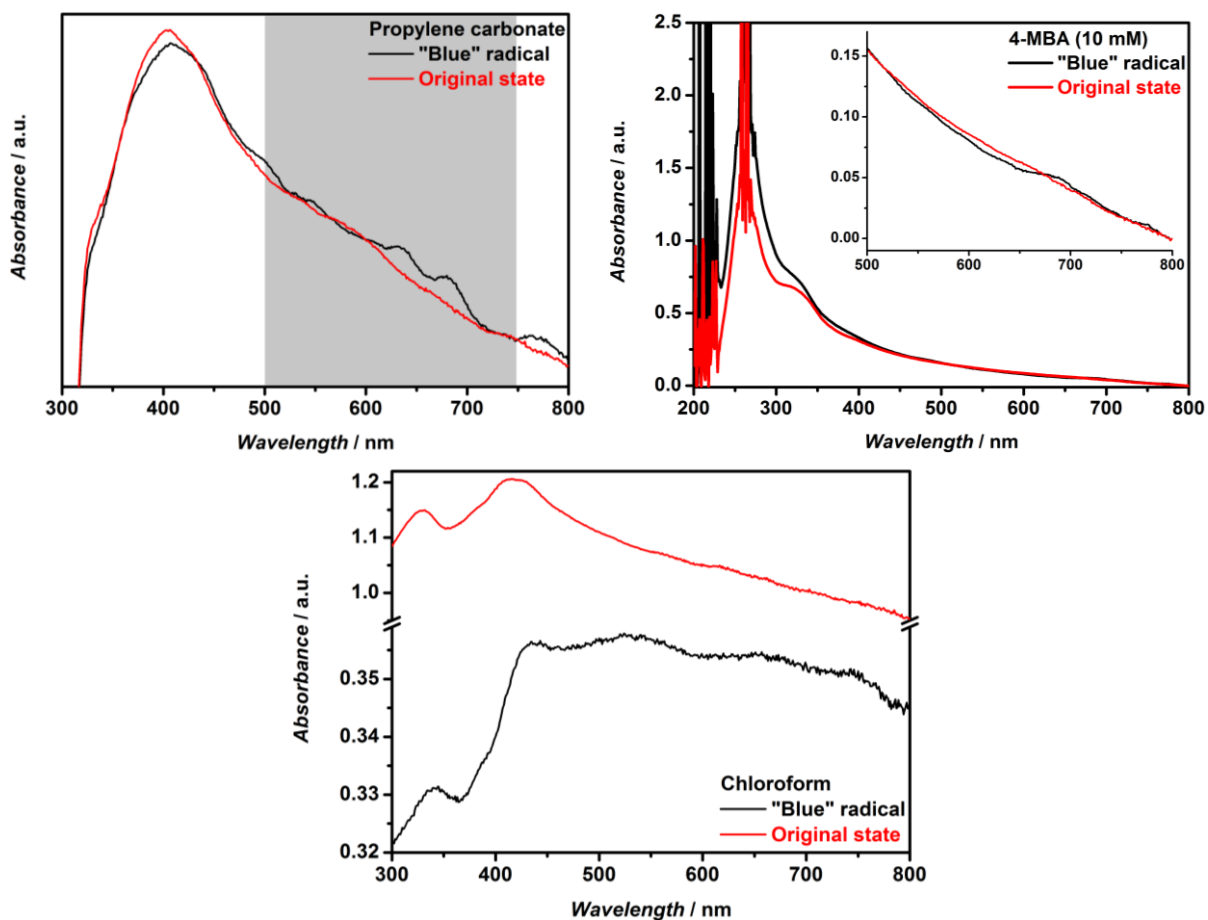# Spectroscopic characterisation of the blue radical

Figure S4 Transmission UV-Vis spectra of the NCN-CN$_x$ in its blue radical state and its non-reduced, yellow state suspended in propylene carbonate (top left), an aqueous solution of 4-MBA (top right), and chloroform (bottom). The gray area (top left) shows the region where the distinct three-band pattern of the blue radical from 1,4-dicyanamidobenzene dianion manifests (see main text).

DFT computations and supplementary EPR characterisations
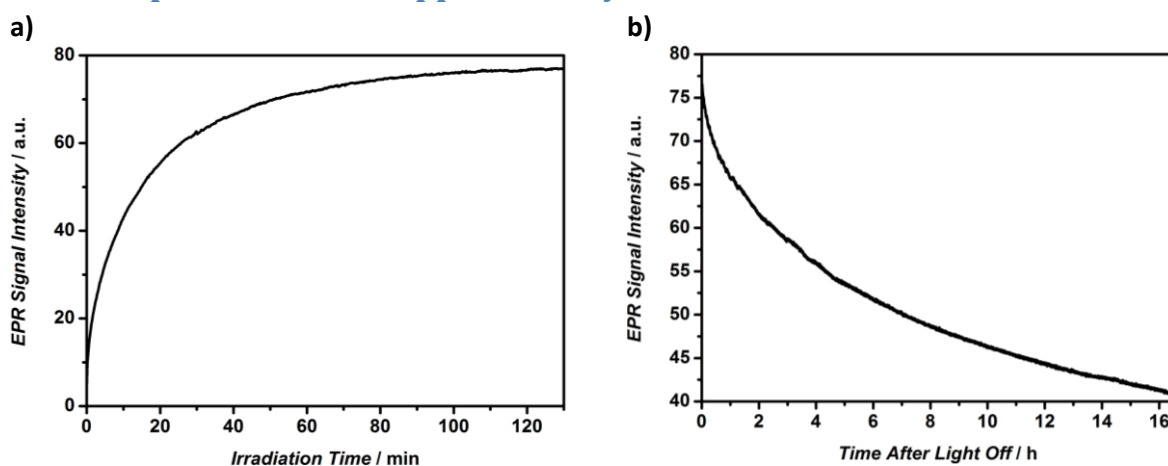
a)

b)

Figure S5 a) Growth of the EPR signal with increasing irradiation time, and b) decay of the EPR signal after cessation of irradiation.

All DFT computations were performed with the ORCA package version 3.03.[3] Since the computations were exploratory and a large structural space was considered, medium-sized basis sets (DZP for geometry optimization and *g* tensor computations, EPRII for computation of hyperfine couplings) were used together with the pure density functional BP86. Geometry optimization was performed within the spin-restricted Kohn-Sham formalism, while EPR parameters were computed with the spin-unrestricted Kohn-Sham formalism. For a few cases, EPR parameters were recomputed with different functionals, including the hybrid B3LYP functional, and larger basis sets (EPRIII for hyperfine and nuclear quadrupole couplings and TZVPP for the *g* tensor). Changes in the parameters were significant, but much smaller than the differences that are discussed in the following for radical assignment. For anion radicals with six or more triazine or heptazine units, problems were encountered with convergence of the self-consistent field (SCF) procedure. In geometry optimizations these problems were solved by applying an energy shift of 0.25 Hartree to the virtual orbitals. For computations of EPR parameters, we used the SlowConv keyword of ORCA, in some cases followed by the Newton-Raphson procedure to achieve very tight convergence in a reasonable time.

Scheme S1 portrays the structure space that was explored. The main questions were related to the ^{14}N hyperfine coupling and nuclear quadrupole interaction that we observed experimentally by HYSCORE spectroscopy. We inquired whether a radical localized in the NCN group or in a triazine unit or in a heptazine unit was consistent with these parameters. Furthermore, we asked what extent of delocalization of the unpaired electron would lead to the observed magnitude of the hyperfine coupling and whether this extent of delocalization could be observed when a neutral or charged diamagnetic polymer was reduced by transfer of one electron. As polymer mimics we considered the cyclic hexamer **3** shown in Scheme S1 that tends to remain planar in most charge states and with most side group combinations and an analogous hexamer made up of triazine units, which undulates as a tetraanion radical with the three inner amine bridges being deprotonated and with $-NH_2$ side groups on the outer rim. We also included triazine and heptazine hexamers and decamers without ring closure and with and without charge-neutral or anionic cyanamide side groups. For 1D oligomers, even when starting from a planar structure pre-optimized with the MMFF94 force field, DFT-optimized structures of anion radicals were non-planar (torsion angles up

to 10° between neighboring units). This effect was even stronger when amine bridges were deprotonated. Torsion angles of about 50-60° were observed in the latter case.

We tested for possible localization of the unpaired electron in a neutral or negatively charged cyanamide group. Such localization is not observed in any model compound within the structure space described in Scheme S1. It can only be achieved if the cyanamide group is linked to an sp^3 carbon atom, for instance a methyl group, instead of a triazine or heptazine unit. When it is linked to a triazin unit (**2a**, **2b**) or heptazine unit (**1a**, **1b**), most spin density is found in the heterocycles. If the spin is localized in the cyanamide group, large isotropic ^{14}N hyperfine couplings are observed that are in disagreement with the W-band CW EPR spectrum and none of the two ^{14}N hyperfine coupling tensors matches the one observed in the HYSCORE spectrum. Therefore, we can conclude that the unpaired electron resides in triazine or heptazine units.

Models with triazine or heptazine units feature a large number of nitrogen atoms, in particular, the hexamers and decamers. For comparison with the HYSCORE experiment, we consider the atoms with a hyperfine coupling that comes closest to the exact cancellation condition, where the hyperfine coupling $A(^{14}N)$ matches twice the nuclear Zeeman frequency ν_I at W-band frequencies $A(^{14}N) \approx 20$ MHz). This condition does not only lead to the largest modulation depth in ESEEM and HYSCORE experiments, it also causes substantial line narrowing.[4] Hence, the nuclei with hyperfine coupling close to this condition strongly dominate HYSCORE spectra. In line with this reasoning we observed a ^{14}N hyperfine tensor with $A_{||}$ = 18.0 MHz and $A_\perp$ = 0.9 MHz that is close to exact cancellation near its unique axis direction and has an isotropic component of 6.6 MHz that is not too far from exact cancellation. To be consistent with experimental findings, any assignment should also reproduce axial symmetry of the hyperfine tensor, the ^{14}N nuclear quadrupole coupling of $|Q|$ = 3.2 MHz (the sign cannot be inferred from the spectrum) and the asymmetry parameter η = 0 corresponding to axial symmetry of the nuclear quadrupole tensor. An overview of the EPR parameters of the most relevant nuclei in each species is given in Table S2. Species are classified by the type of repeat units and side groups, according to Scheme S1, by the number n of repeat units in the oligomer and by their total charge. Note that one negative charge arises from assuming one-electron reduction of the monomer by an electron transfer process. Additional negative charges correspond to deprotonation of amine bridges or cyanamide side groups.
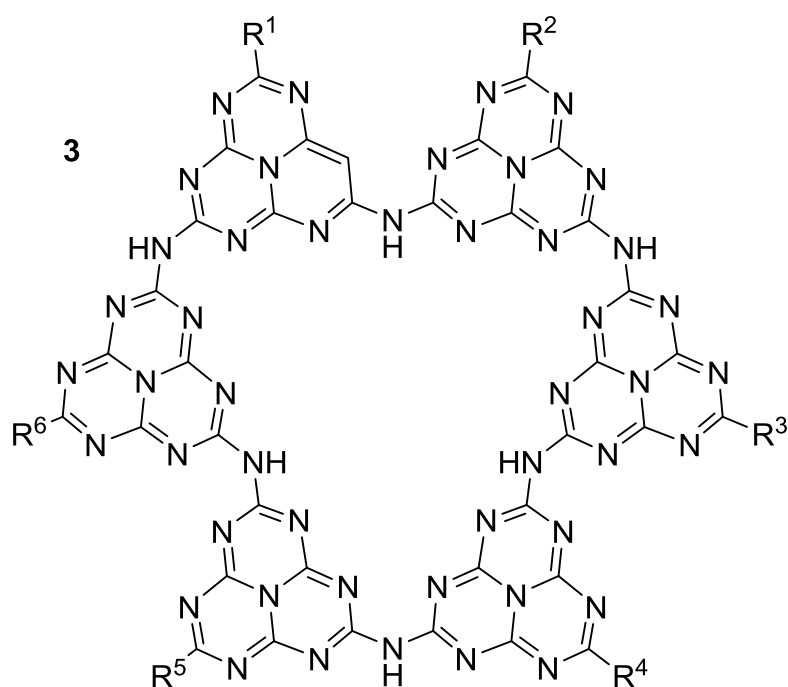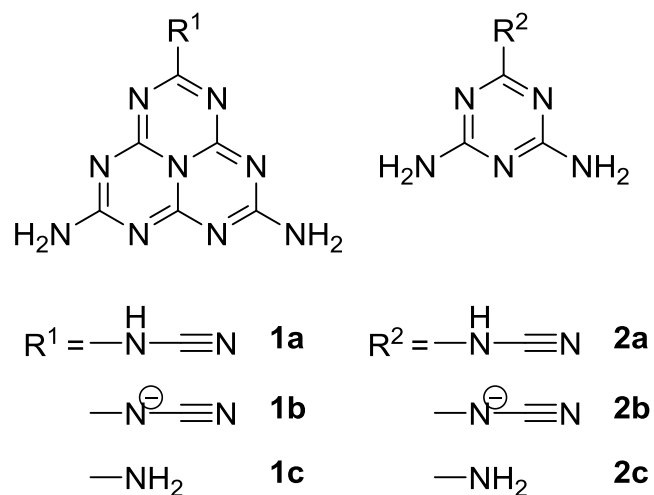
Scheme S1 Structural motifs considered in DFT computations. Heptazine units **1** and triazine units **2** were considered as repeat units of the polymer and were linked via the amino groups. Linking groups were considered in the protonated charge-neutral form (-NH-) or in the deprotonated anionic form. Neutral or anionic NCN side groups were attached in some cases. As the smallest motif for emulating a two-dimensional polymer, we considered the cyclic hexamer **3** with various combinations of side groups R^1-R^6.

Monomer	n	Charge	A_x/ MHz	A_y/ MHz	A_z/ MHz	Q/ MHz	η	g_x	g_y	g_z
1a	1	-1	-1.8	-1.9	25.3	-3.9	0.02	2.0022	2.0026	2.0030
1a[a]	1	-1	-1.8	-1.9	26.1	-3.9	0.01	2.0022	2.0027	2.0032
1a[b]	1	-1	0.9	1.0	29.6	-4.1	0.01	2.0022	2.0026	2.0031
1b	1	-2	-0.7	-0.9	23.9	-3.9	0.03	2.0022	2.0027	2.0031
1c	1	-1	2.9	2.9	31.0	-4.0	0.00	2.0021	2.0028	2.0028
2a	1	-1	-16.0	-13.6	4.0	-4.1	0.21	2.0005	2.0020	2.0053
2b	1	-2	-14.7	-13.2	5.3	-3.5	0.49	2.0003	2.0021	2.0053
2c	1	-1	-18.0	-15.9	2.0	-3.9	0.29	2.0005	2.0020	2.0056
1c	2	-1	-1.6	-1.7	13.6	-3.1	0.04	2.0022	2.0028	2.0032
1c	2	-2[c]	-1.6	-1.7	14.5	-3.2	0.14	2.0022	2.0027	2.0028
1a/1b	2	-2	-2.7	-2.7	25.6	-3.7	0.04	2.0022	2.0027	2.0030
1b/1c	2	-2	-2.7	-2.7	26.3	-3.5	0.03	2.0022	2.0027	2.0030
2c	2	-1	-2.4	-2.5	12.7	2.7	0.43	2.0023	2.0030	2.0036
			-7.0	-8.0	-11.4	-3.3	0.22	-	-	-
2c	2	-2[c]	-2.4	-2.5	13.2	2.7	0.17	2.0023	2.0029	2.0032
			-3.9	-5.2	-11.2	-3.8	0.48	-	-	-
2b/2c	2	-2	-3.8	-3.9	-16.6	2.9	0.29	2.0023	2.0026	2.0033
			-5.5	-5.9	-6.2	-3.6	0.21	-	-	-
1c	6	-1	-0.6	-0.6	4.8	-2.8	0.03	2.0023	2.0033	2.0033
1c[d]	6	-4	-0.5	-0.5	5.0	-2.9	0.18	2.0023	2.0030	2.0030
1a(3)/**1b**(3)[e]	6	-4	-0.8	-0.8	7.3	-2.9	0.08	2.0024	2.0032	2.0032
1a(2)/**1b**(4)[f]	6	-5	-1.5	-1.6	13.3	-3.2	0.08	2.0024	2.0029	2.0030
1a(1)/**1b**(5)	6	-6	-2.2	-2.2	21.1	-3.6	0.07	2.0024	2.0030	2.0032
1a[g]	6	-1	-0.6	-0.6	5.8	-2.7	0.05	2.0023	2.0029	2.0032
1a(1)/**1b**(5)[g]	6	-6	-1.7	-1.8	16.5	-3.4	0.06	2.0023	2.0030	2.0033
2c	6	-1	-1.2	-1.2	4.8	-2.9	0.84	2.0023	2.0037	2.0037
2c[f]	6	-4	-1.1	-1.2	4.8	-2.5	0.55	2.0021	2.0034	2.0035
2a(3)/**2b**(3)[e]	6	-4	-1.2	-1.3	5.1	-2.5	0.78	2.0022	2.0037	2.0037
2b(3)/**2c**(3)[e]	6	-4	-1.1	-1.2	4.3	-2.9	0.86	2.0023	2.0037	2.0037
1c	10	-1	-0.8	-0.8	7.6	-2.8	0.01	2.0023	2.0030	2.0032
1c[h]	10	-3	-0.9	-0.9	6.2	-3.0	0.06	2.0026	2.0031	2.0034
2c	10	-1	-1.7	-1.7	8.0	-2.9	0.82	2.0022	2.0032	2.0037
2c[h]	10	-3	-1.5	-1.5	7.7	2.7	0.63	2.0025	2.0031	2.0036

[a]basis set EPRIII for hyperfine couplings, TZVPP for *g* tensor computation, BP86 functional

[b]basis set EPRIII for hyperfine couplings, TZVPP for *g* tensor computation, B3LYP functional

[c]amine bridge deprotonated

[d]inner amine bridges deprotonated

[e]alternating neutral and charged monomers

[f]two adjacent neutral monomers

[g]linear oligomer

[h]two amine bridges deprotonated

The monomeric heptazine species (**1a**, **1b**, **1c** with *n* = 1) have somewhat larger hyperfine and nuclear quadrupole couplings than are experimentally observed, whereas symmetry of the two tensors matches nicely with the experimental observations. The relevant nucleus is the central nitrogen atom of the heptazine unit. In contrast, the monomeric triazine species (**2a**, **2b**, **2c** with *n* = 1) exhibit a hyperfine tensor with a small coupling along the *z* direction and two large absolute values of the coupling along *x* and *y*, which qualitatively disagrees with the HYSCORE spectrum.

Furthermore, they each have two ^{14}N nuclei with a large isotropic hyperfine coupling (40-50 MHz, not shown in Table S2) that is inconsistent with the W-band CW EPR spectrum.

Dimeric heptazine species without cyanamide groups (**1c**) have a somewhat too small hyperfine coupling, although it could be argued that the difference to experiment is within the accuracy of the DFT computations. In the case of the anion radical (**1c**, n = 2, charge -1) we checked that a computation with larger basis set (BP86/EPRIII level) does only lead to moderate changes (hyperfine tensor principal values of -1.5, -1.6, 14.3 MHz) that are much smaller than the remaining deviation from experiment. Symmetry and magnitude of the nuclear quadrupole coupling agree with experiment, in particular for the anion radical of the **1c** dimer. If a single, negatively charged cyanamide group is attached to such a dimer, the hyperfine coupling increases almost to the magnitude observed in the monomer (**1a/1b** and **1b/1c**, n = 2, charge -2). Whether the charge-neutral side group is a cyanamide or amino group does not make much difference for the EPR parameters. Closer inspection shows that this increased hyperfine coupling is due to a localization of almost the entire spin density in the heptazine unit that does not carry the anionic cyanamide group-spin avoids charge. This effect is further discussed below.

In dimeric triazine species without cyanamide groups (**2c**) one type of ^{14}N nuclei exhibits nearly axial hyperfine tensors of similar magnitude as the central nitrogen in dimeric heptazine species. However, in the triazine case the nuclear quadrupole coupling deviates significantly from axial symmetry and, furthermore, for a second type of ^{14}N nuclei is significantly closer to exact cancellation and has much smaller hyperfine anisotropy. This second type should be visible in the HYSCORE spectra, but is not observed. This second type corresponds to the bridging amine nitrogen and, accordingly, the nuclear quadrupole parameters change significantly when the bridge is deprotonated. Attachment of an anionic cyanamide group to one of the triazine units (**2b/2c**, n = 2, charge -2) shifts more spin density into the other triazine unit, but this effect is much less dramatic than in the case of heptazine units. The hyperfine tensor of the bridging nitrogen becomes almost isotropic.

In the cyclic hexamer of heptazine units (**1c**, n = 6, charge -1) the hyperfine tensor of the central nitrogen atom is reduced by almost a factor of three compared to the corresponding dimer and nuclear quadrupole coupling is slightly reduced. The decrease in hyperfine coupling is explained by an even distribution of spin density over all six repeat units (Figure S6a). Such an even distribution and virtually perfect planar geometry of the hexamer are observed in spite of not enforcing symmetry during geometry optimization. In each heptazine unit, the central nitrogen is still the one that bears most spin density. If the hexamer is further charged by deprotonating the three inner amine bridges (**1c**, n = 6, charge -4), only small changes are observed, the only significant one being a slight deviation of the nuclear quadrupole coupling from axial symmetry.

If anionic cyanamide groups are attached to heptazine units in the hexamer, spin avoids these units, as was observed for the dimer. Note that, in the hexamer case, we have also attached cyanamide groups to the remaining units, but in the charge-neutral form. The hyperfine coupling in these neutral units increases. With only two adjacent neutral units (**1a**(2)**/1b**(4)) it is almost as large as in the dimer without any side groups, whereas with only one neutral unit (**1a**(1)**/1b**(5)) it is somewhat smaller than in the monomer with a charge-neutral cyanamide side group (**1a**). In the latter case, the hyperfine coupling is also smaller than in a dimer with one anionic and one neutral cyanamide group

(**1a/1b**). These reductions are due to minor delocalization of the unpaired electron into neighbouring anionic units as is also apparent in the spin density plots in Figure S6b,c. Again, only a much smaller preference for charge-neutral groups is observed with triazine units, with an only slightly hyperfine enhancing effect of charge-neutral cyanamide side groups (**2a**(3)**/2b**(3)) and a dehancing effect of amino side groups (**2b**(3)**/2c**(3)). Charging the amine bridges between triazine units by deprotonation (**2c**, n = 6, charge -4) causes only insignificant changes in the hyperfine coupling and small changes in the nuclear quadrupole coupling compared to the case with charge-neutral bridges (**2c**, n = 6, charge -1).
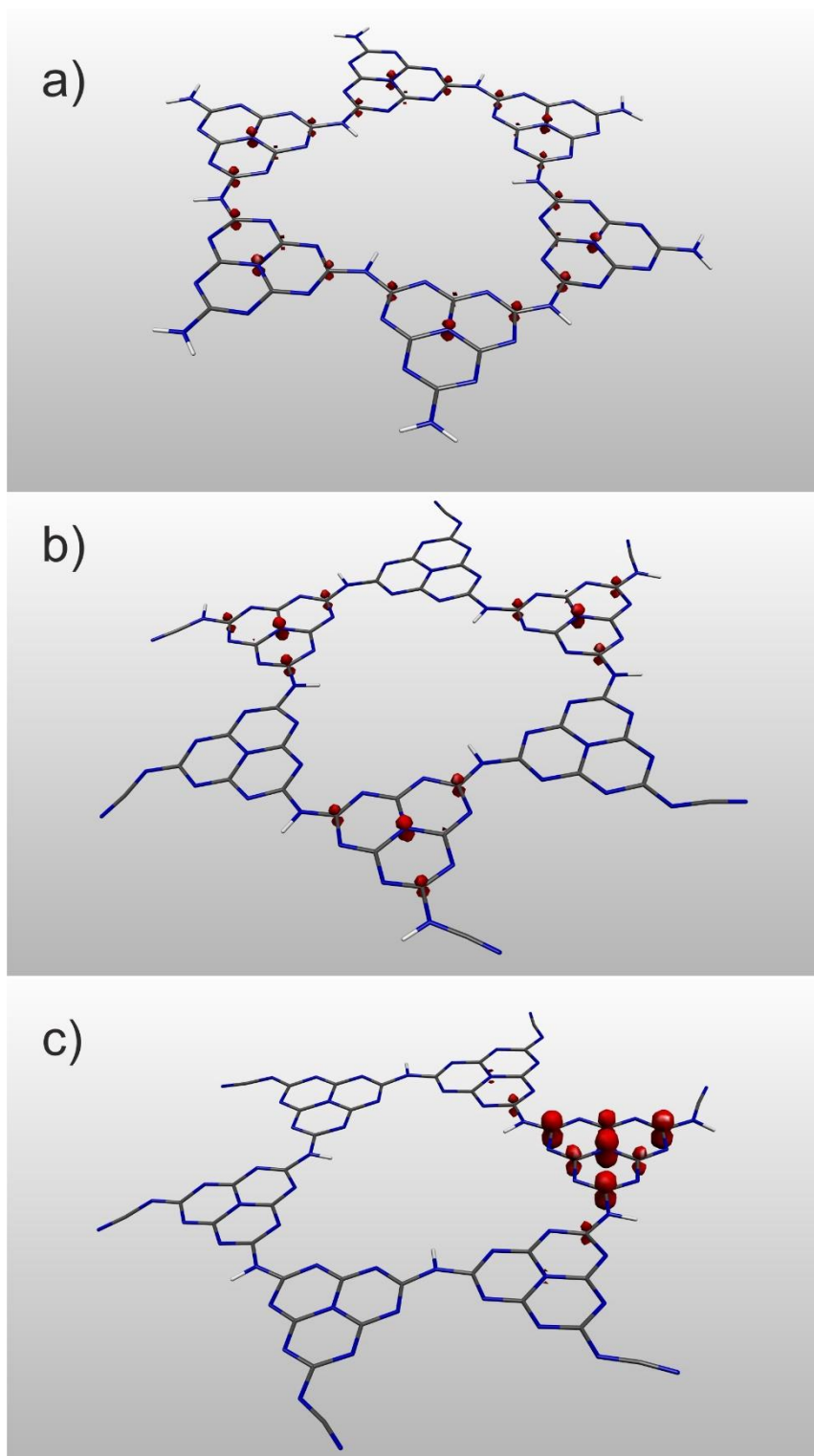
Figure S6 Spin density distribution in cyclic heptazine hexamers. a) Anion radical with amino side groups. b) Tetraanion radical with three charge-neutral and three anionic cyanamide side groups. Spin density is localized in the units with charge-neutral side groups. c) Hexaanion radical with one charge-neutral and five anionic cyanamide side groups. Spin density is strongly localized to the single unit with charge-neutral side group.

In a linear heptazine hexamer with six neutral cyanamide side groups (**1a**, n = 6, charge -1), the repeat units at the chain ends have slightly less spin density, which leads to a somewhat larger ^{14}N hyperfine coupling of the central nitrogen in the four inner repeat units compared to the cyclic hexamer without cyanamide side groups (**1c**, n = 6, charge -1). However, the observed coupling is

still by a factor of three smaller than the one experimentally observed in the HYSCORE spectra. Again, spin avoids charge if some of the cyanamide side groups are deprotonated. If only a single cyanamide group is in a charge-neutral protonated state (**1a**(1)/**1b**(5) n = 6, charge -6), the hyperfine tensor and nuclear quadrupole tensor of the central ^{14}N nucleus in the corresponding repeat unit match the experimental result within the combined accuracies of the spectral simulation and DFT computation. Likewise, the principal values of the g tensor match within this accuracy.

In the non-planar heptazine decamers (**1c**, n = 10, charge -1 and -3) the unpaired electron is less delocalized than in the corresponding planar hexamers. Closer inspection shows that the spin density resides mostly on only two heptazine units, but there is sufficient delocalization to other units to reduce the hyperfine tensor of the central nitrogen atom of the heptazine units to a significantly smaller magnitude than found in dimers. Although the charged amino bridges lead to even larger dihedral angles between heptazine units, they slightly enhance rather than reduce delocalization, as is apparent from the slightly smaller hyperfine coupling. Similar effects are seen for the triazine case (**2c**, n = 10, charge -1 and -3).

The g tensor principal values are less discriminating between different radical structures than the maximum ^{14}N hyperfine coupling. Nevertheless, except for the triazine-based dimers with one anionic cyanamide group (**2c**, n = 2, charge -2; **2b/2c**, n = 2, charge -2) all triazine-based radicals have a maximum g tensor principal value that significantly exceeds the largest g value observed experimentally. The g tensor principal values of heptazine-based radicals with cyanamide side groups vary approximately in the range observed experimentally as g strain.

Regarding the assignment, a triazine-based polymer is hard to reconcile with observations in the HYSCORE spectrum. One of the hyperfine tensors in a triazine dimer roughly matches the one observed, but it would be hard to explain why the bridging nitrogen, which has a hyperfine coupling even closer to exact cancellation, is not observed. Furthermore, the quadrupole coupling of the ^{14}N nucleus, whose hyperfine coupling roughly matches, is significantly off from the axial symmetry observed experimentally. Finally, and maybe most importantly, it is impossible to extend from the dimer and still keep the hyperfine coupling sufficiently large to be consistent with experiment.

Notably, the latter problem does not occur for a heptazine-based polymer. Depending on the pattern of charge-neutral and anionic cyanamide sidegroups in neighbouring units, a heptazine unit with a charge-neutral cyanamide side group in a polymer is found to have slightly larger or slightly smaller hyperfine couplings than observed experimentally and a nearly axial nuclear quadrupole interaction of the experimentally observed magnitude. It is reasonable to assume that in a random heptazine polymer with some anionic cyanamide side groups charge-compensated by potassium ions and some charge-neutral cyanamide side groups, part of the unpaired electrons will be pinned to one or two heptazine units because they are isolated from other neutral units by units with anionic side groups. Of course, other parts of the polymer chain or other chains would then carry radicals that are more delocalized and have smaller hyperfine coupling. Such radicals would not significantly contribute to the HYSCORE spectrum, as their hyperfine coupling is much further from exact cancellation. Yet, there is experimental evidence that such radicals with smaller hyperfine couplings must exist. If all radicals were of the type observed by HYSCORE, the CW EPR spectrum would exhibit a ^{14}N hyperfine splitting that is not observed. Furthermore, both transverse and longitudinal relaxation times are surprisingly short for organic radicals, which indicates significant

spin-spin interaction between these radicals. Because dipole-dipole broadening of the CW EPR line is weak, if any is present, radical-radical interaction is expected to have exchange contributions that stem from minor overlap of the singly occupied molecular orbitals. Radicals similar to the ones in the linear oligomers shown in Figure S7 would be consistent with such a scenario.
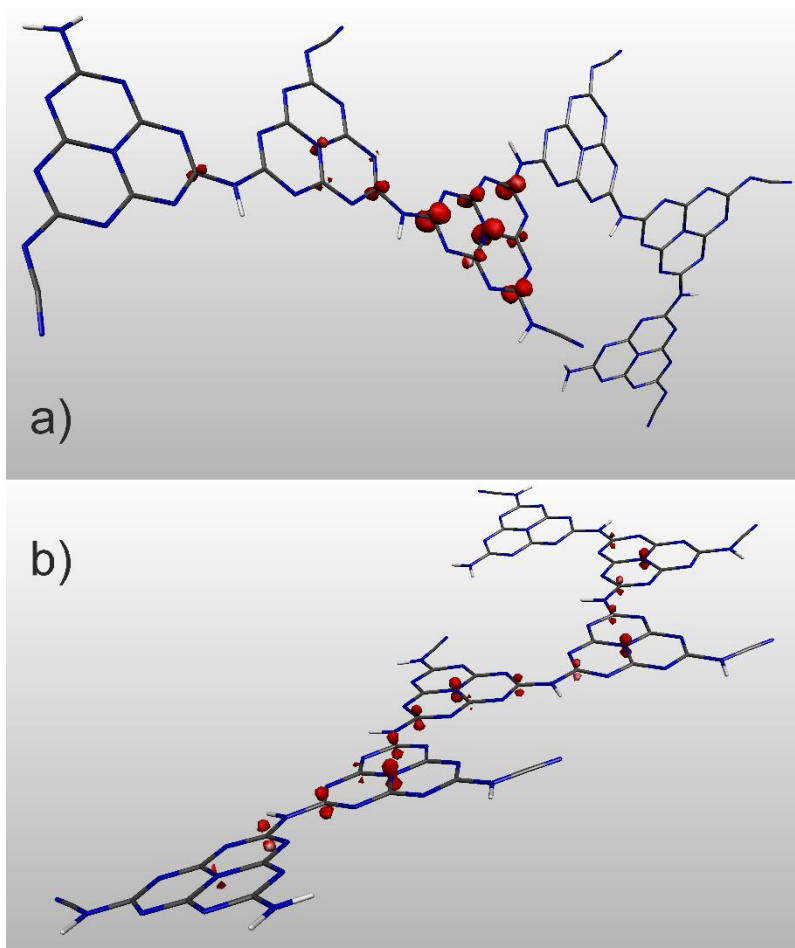

Figure S7 Spin density distribution in linear heptazine hexamers. a) Model 1a(1)/1b(5) *n* **= 6, charge -6. Spin density is localized mainly in the only heptazine unit that has a charge-neutral cyanamide side group. b) Model 1a,** *n* **= 6, charge -1. Spin density is almost equally distributed over the four inner heptazine units.**

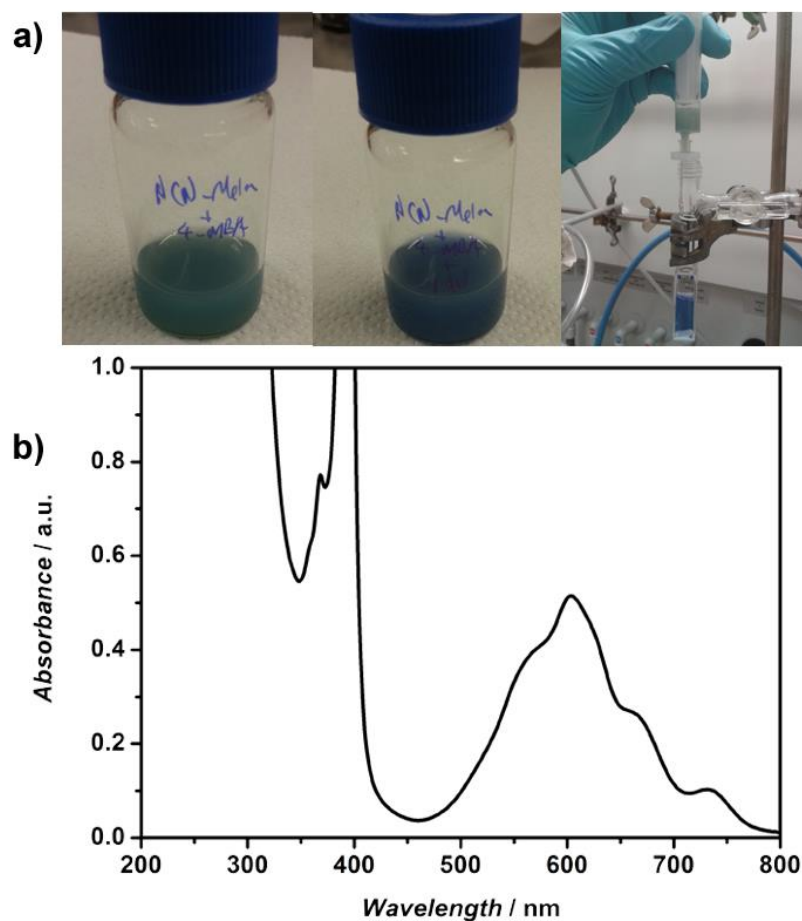# (Photo)electrochemical characterization of the blue radical

Figure S8 a) Photographs showing the formation of the blue radical by irradiating NCN-CN$_x$ suspended in an aqueous solution of 4-MBA in oxygen-free conditions (left), after addition of a colourless MV^{2+} solution under oxygen-free transfer to yield the blue MV$^{+\bullet}$ radical (middle), and isolation of the blue MV$^{+\bullet}$ solution by filtering out the NCN-CN$_x$ particles through a syringe filter into a Schlenk cuvette (right). **b)** UV-Vis spectrum of the blue MV$^{+\bullet}$ solution.

Table S3 Electrochemical induction of the blue radical state of a film of NCN-CNx on FTO as a function of applied potential

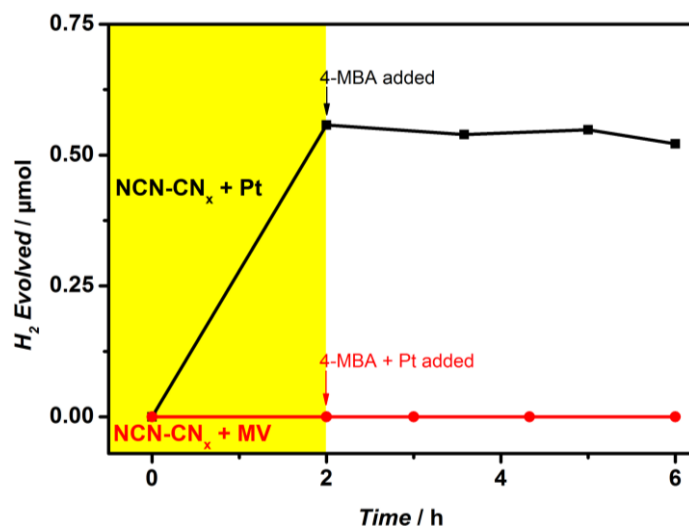| Applied potential (mV vs NHE)	Observed colour
-380	Yellow/white
-480	Yellow/white
-530	Slightly blue
-580	Intense blue

Figure S9 Control experiment for the dark hydrogen evolution, where the region highlighted in yellow indicates AM1.5 irradiation while the part without highlight indicates a light-free environment. Here, a suspension of NCN-CN$_x$ (20 mg) in PBS (10 mL, pH 7, 1 M) with either platinum colloid (black plot) or MV (red plot) was irradiated for 2 h and no colour change was observed. After removing the reactor from the irradiation, 4-MBA (24 mg) in PBS (10 mL, pH 7, 1 M) without and with the platinum colloid (black and red plot respectively) was injected under air-free handling.
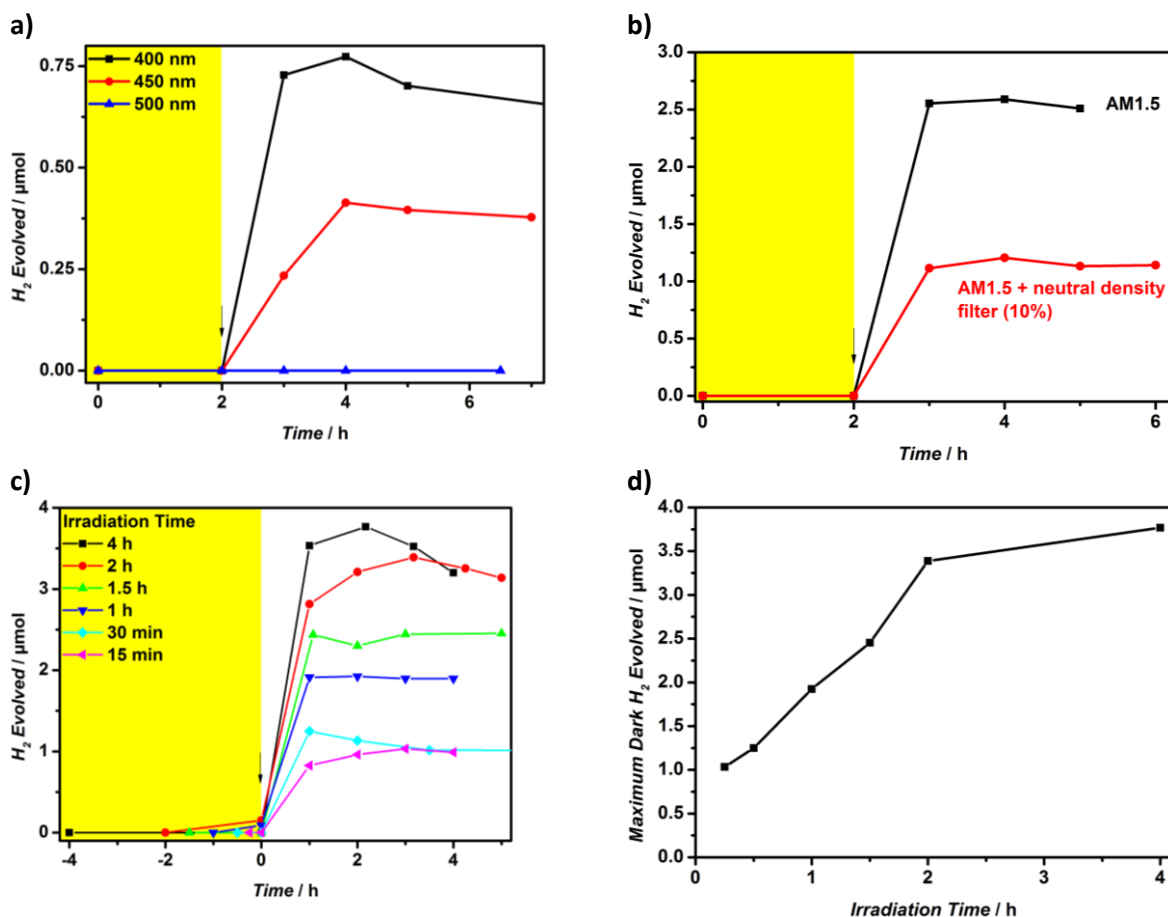

Figure S10 Time versus hydrogen evolution plots with variations in the irradiation source (a), irradiation intensity (b), and irradiation time (c). The yellow band shows the period under irradiation and the arrow indicates the point at which the platinum colloid (50 µL of 1000 ppm solution) was added. d) Summary of how the maximum dark hydrogen evolved changes with irradiation time in c).
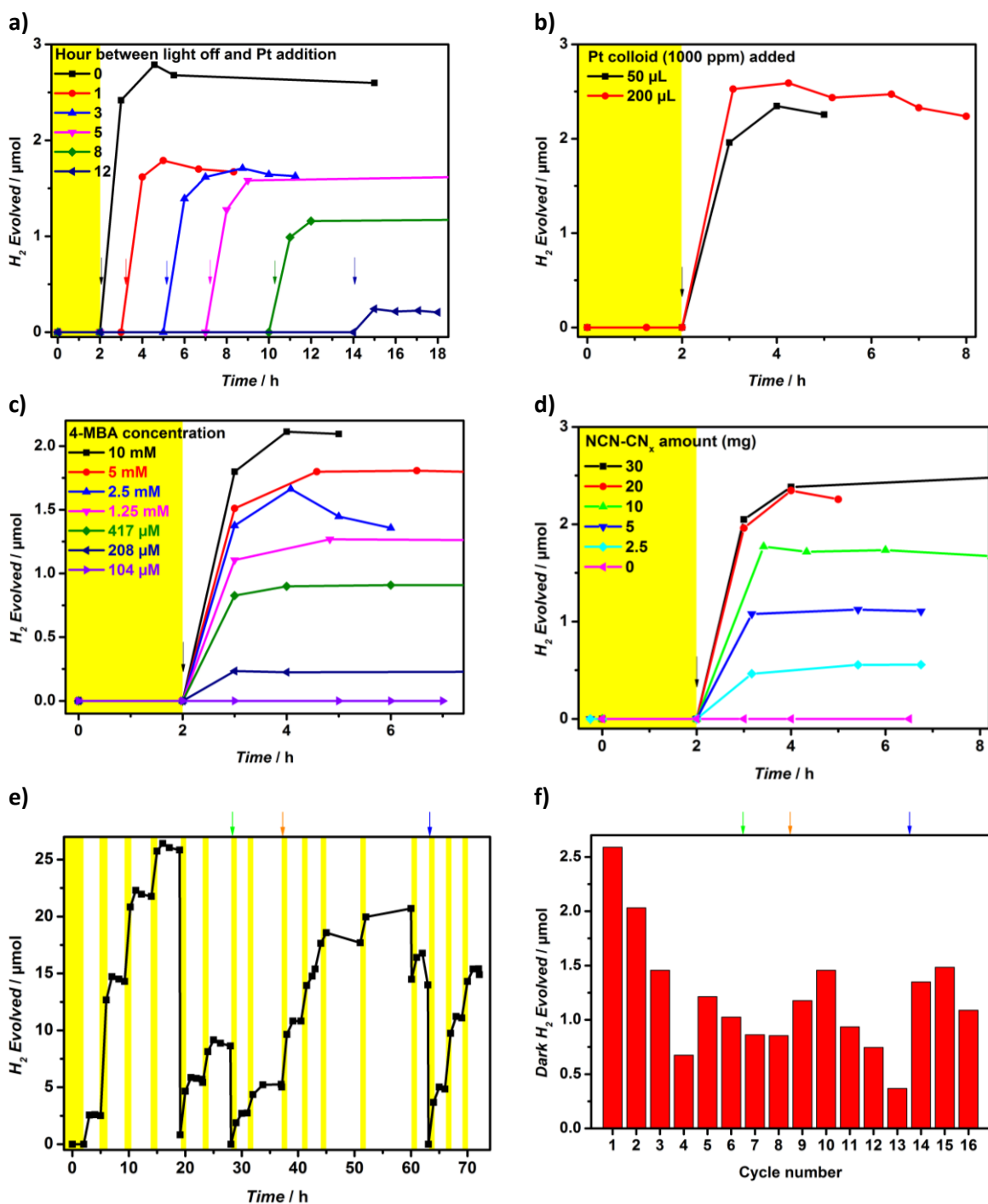
Figure S11 Time versus hydrogen evolved plots with variations in a) time between light off and injection of Pt colloid; b) amount of Pt colloid injected; c) amount of 4-MBA; d) amount of NCN-CN$_x$, and e) repeated cycles testing the durability of NCN-CN$_x$ for dark hydrogen evolution. Dark hydrogen evolved based on the cycle number is summarized in f). For all plots, the yellow band shows the period under irradiation, and data points beyond 8 h are not shown. Except in e), the arrow indicates the point at which the Pt colloid (50 µL of 1000 ppm) was added. For e) and f), the green arrow indicates the addition of 4 –MBA (6 mg), the orange arrow the addition to Pt colloid (50 µL), and the blue arrow the addition of both 4-BMA (24 mg) and Pt colloid (50 µL).

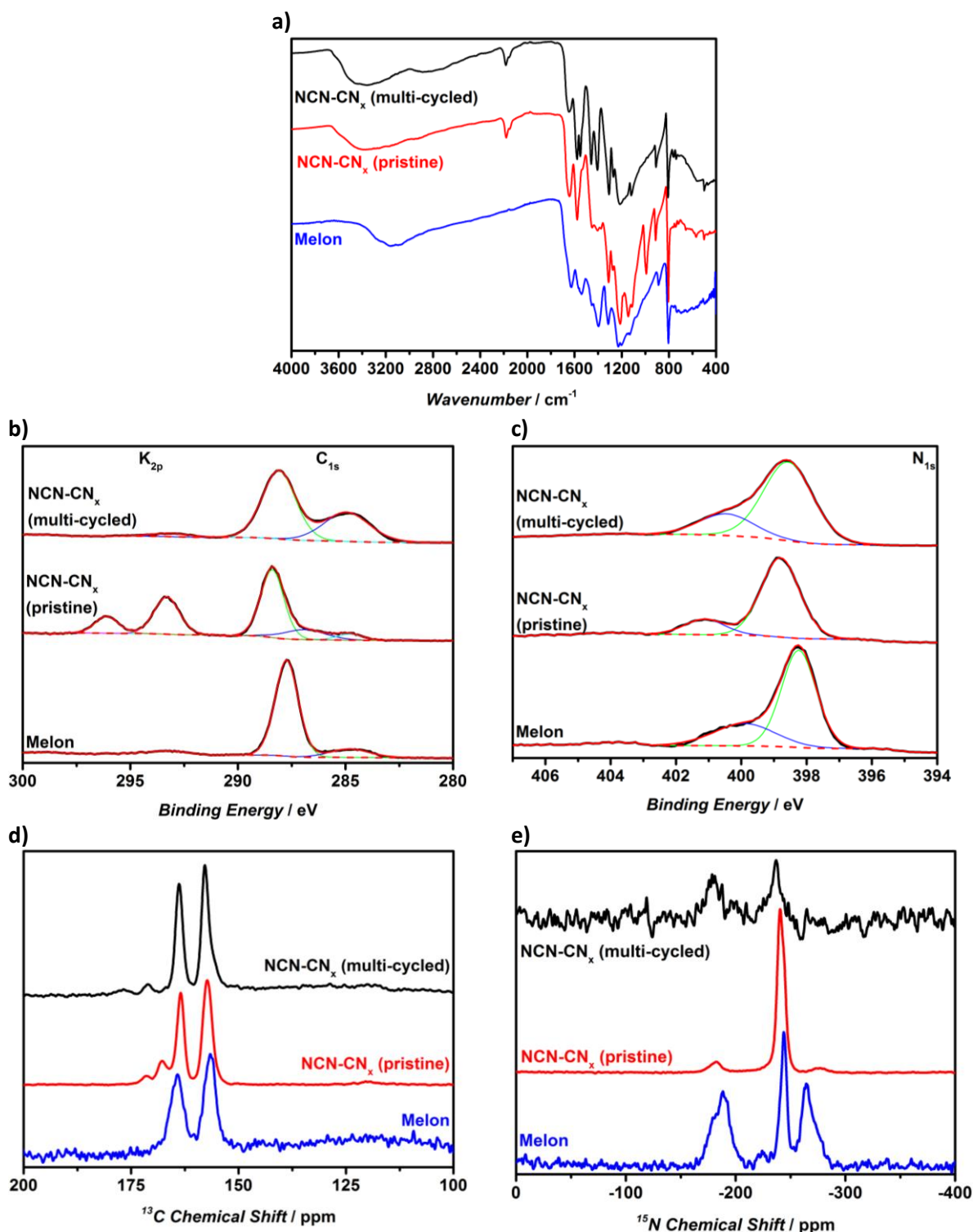# NCN-CN$_x$ after repeated dark hydrogen evolution experiments

Figure S12 Characterisation of the NCN-CN$_x$, isolated by centrifugation and extensively washed with water, after repeated dark hydrogen evolution: a) FTIR; b) XPS in the C$_{1s}$ and K$_{2p}$ region; c) XPS in the N1s region; d) solid state MAS NMR for ^{13}C direct excitation, and e) ^{15}N cross polarisation. All characterisations are shown with the pristine NCN-CN$_x$ and melon for comparison.

The amount of dark hydrogen evolved decreased as the dark photocatalytic hydrogen evolution process is repeatedly cycled. Re-supplying more 4-MBA (before cycle 7) did not increase the amount of dark hydrogen evolved, but adding platinum colloid (before cycle 9) restored the activity to that of the 3rd cycle, which is around 60% that of the 1st cycle. This suggests that the dark hydrogen

evolution process for NCN-CN$_x$ is principally limited by the platinum colloid likely caused by poisonous by-product(s) produced in the oxidation of the electron donor, or loss of contact between the catalyst and the co-catalyst. Characterisation of the NCN-CN$_x$ after isolation and extensively washing with water (Figure S9) indicates partial hydrolysis of the cyanamide unit to urea with concomitant loss of K$^+$ (Figure S9b), which may cause the decrease of dark hydrogen evolved following the first two cycles.

References

[1] V. W.-h. Lau, I. Moudrakovski, T. Botari, S. Weinberger, M. B. Mesch, V. Duppel, J. Senker, V. Blum, B. V. Lotsch, *Nat. Commun.* **2016**, *7*, 12165.

[2] V. W.-h. Lau, M. B. Mesch, V. Duppel, V. Blum, J. Senker, B. V. Lotsch, *J. Am. Chem. Soc.* **2015**, *137*, 1064-1072.

[3] F. Neese, *WIREs Comput. Mol. Sci.* **2012**, *2*, 73-78.

[4] H. L. Flanagan, D. J. Singel, *J. Chem. Phys.* **1987**, *87*, 5606-5616.